

## ARTICLE OPEN



## Flexible kesterite thin-film solar cells under stress

Ha Kyung Park<sup>1</sup>, Yuna Cho<sup>1</sup>, Juran Kim<sup>1</sup>, Sammi Kim<sup>2</sup>, Sungjun Kim<sup>3</sup>, Jeha Kim<sup>3</sup>, Kee-Jeong Yang<sup>2,✉</sup>, Dae-Hwan Kim<sup>2</sup>, Jin-Kyu Kang<sup>2</sup> and William Jo<sup>1,✉</sup>

Understanding the stress-induced phenomena is essential for improving the long-term application of flexible solar cells to non-flat surfaces. Here, we investigated the electronic band structure and carrier transport mechanism of  $\text{Cu}_2\text{ZnSn}(\text{S},\text{Se})_4$  (CZTSSe) photovoltaic devices under mechanical stress. Highly efficient flexible CZTSSe devices were fabricated controlling the Na incorporation. The electronic structure of CZTSSe was deformed with stress as the band gap, valence band edge, and work function changed. Electrical properties of the bent CZTSSe surface were probed by Kelvin probe force microscopy and the CZTSSe with Na showed less degraded carrier transport compared to the CZTSSe without Na. The local open-circuit voltage ( $V_{\text{OC}}$ ) on the bent CZTSSe surface decreased due to limited carrier excitation. The reduction of local  $V_{\text{OC}}$  occurred larger with convex bending than in concave bending, which is consistent with the degradation of device parameters. This study paves the way for understanding the stress-induced optoelectronic changes in flexible photovoltaic devices.

npj Flexible Electronics (2022)6:91; <https://doi.org/10.1038/s41528-022-00221-4>

## INTRODUCTION

Flexible and lightweight thin-film solar cells hold great promise to be applied as a power source for stretchable, bendable, and foldable electronic devices<sup>1</sup>. Wide research on flexible photovoltaic devices led to the development of the highly efficient and bending tolerant crystalline silicon (c-Si)<sup>2</sup>, chalcopyrite<sup>3–5</sup>, and perovskite<sup>6–8</sup> based flexible solar cells. Investigation of various flexible substrate materials, such as polymers, flexible glasses, and metal foils, has been conducted to improve the flexibility and functionality of flexible solar cells<sup>9,10</sup>. Furthermore, stable light-absorbing materials have drawn attention as candidates for durable devices<sup>11</sup>. Additionally, electrical properties in bent photovoltaic devices should be studied to maximize the performance of stable and highly efficient flexible devices.

Earth-abundant kesterite materials [ $\text{Cu}_2\text{ZnSnS}_4$  (CZTS),  $\text{Cu}_2\text{ZnSnSe}_4$  (CZTSe), and  $\text{Cu}_2\text{ZnSn}(\text{S},\text{Se})_4$  (CZTSSe)] are promising alternatives to c-Si and  $\text{Cu}(\text{In},\text{Ga})(\text{S},\text{Se})_2$  (CIGS) for lightweight thin-film solar cells owing to their nontoxicity and low cost. The band gap of these materials can be tuned (from 1.0 to 1.5 eV) by adjusting the ratio of S and Se, and their absorption coefficient (approximately  $10^4 \text{ cm}^{-1}$ ) is high<sup>12,13</sup>. Kesterite CZTSSe thin-film solar cells have reached power conversion efficiencies (PCE) of 12.6% with a two-step hydrazine-based non-vacuum fabrication process and that of 12.62% with sputtering<sup>14,15</sup>. In addition, CZTSe thin-film solar cells have recorded PCE of 12.5% by sputtering metallic precursors<sup>16</sup>.

However, the narrow phase stability of kesterite materials results in the formation of secondary phases and defects, which adversely affect the performance of the device. Hence, controlling the secondary phases and defects is crucial to improving efficiency<sup>17–21</sup>. Therefore, research has focused on the positive effect of alkali dopants to overcome these limitations; it revealed that they could suppress the formation of intrinsic defects<sup>22–24</sup>. Additionally, artificial doping with alkali elements was found to be effective in improving the cell performance in a flexible substrate that does not contain an alkali element<sup>25–27</sup>. Particularly, using Na

as a dopant and optimizing the doping conditions increases the efficiency of flexible CZTSSe thin-film solar cells significantly<sup>28,29</sup>. In our previous study, the efficiency of flexible CZTSSe solar cells with an additional sodium fluoride (NaF) doping layer was as high as 11.19%<sup>30</sup>. For more wide applications of highly efficient flexible CZTSSe devices, it is crucial to understand the stress-induced change in device characteristics under various bending conditions.

This study investigated the implications of Na on the electrical characteristics of flexible CZTSSe photovoltaic devices under mechanical stress. Flexible CZTSSe photovoltaic devices using a metallic precursor with the Sn/Cu/Zn stacking order were prepared on a Mo-coated Mo-foil substrate with and without the additional NaF layer. We applied the mechanical stress to the flexible CZTSSe thin-film solar cells by bending the samples during the measurements. Changes in charge barriers and carrier behavior at the bent material surface were studied by analyzing the local electrical properties. Moreover, the loss of local open-circuit voltage ( $V_{\text{OC}}$ ) in the bending mode was investigated by the carrier excitation mechanism. Furthermore, the degradation of photovoltaic parameters due to the bending (either concave or convex) was explained.

## RESULTS AND DISCUSSION

## Electronic band structure of CZTSSe with stress

Changes in the electronic band structure of CZTSSe were studied to investigate the effect of mechanical bending on material properties. CZTSSe thin-film samples were in the mechanically bending states with the uniform strain for all measurements (Supplementary Fig. 1). The optical band gap was changed under the mechanical bending state compared to the planar state (Fig. 1a, b). The band gap of Na-doped CZTSSe was slightly smaller than that of Na-undoped CZTSSe<sup>30</sup>. For both Na-doped and undoped CZTSSe samples, the band gap decreased in the concave bending state and increased in the convex bending state. Band gap change of Na-undoped CZTSSe in concave and convex

<sup>1</sup>Department of Physics, Ewha Womans University, Seoul 03760, Republic of Korea. <sup>2</sup>Division of Energy Technology, Daegu Gyeongbuk Institute of Science and Technology (DGIST), Daegu 42988, Republic of Korea. <sup>3</sup>Department of Solar & Energy Engineering, Cheongju University, Cheongju 28503, Republic of Korea. ✉email: kjang@dgist.ac.kr; wmojo@ewha.ac.kr

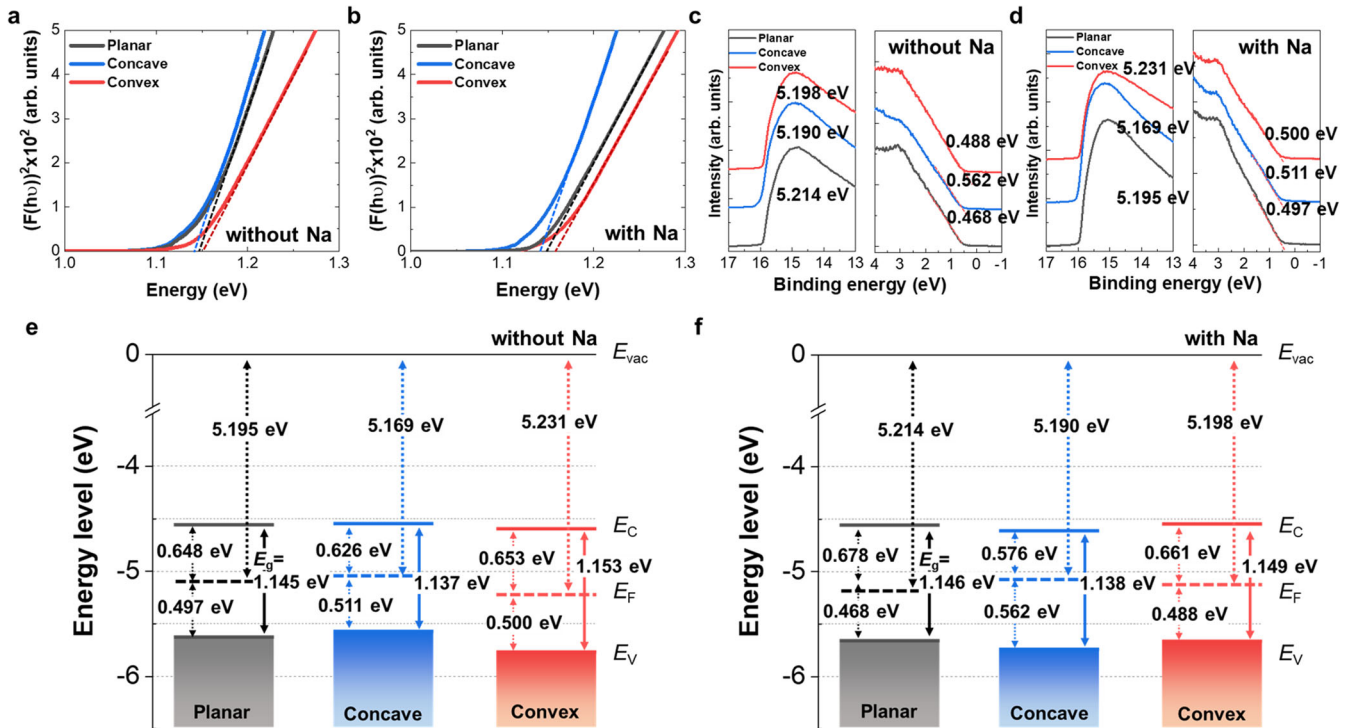


**Fig. 1** Changes in electronic band structure with mechanical stress. **a, b** Tauc plot obtained from diffuse reflectance spectroscopy (DRS). **c, d** Valence band edge and work function of CZTSSe (**c**) without and (**d**) with Na elements under planar, concave, convex bendings. **e, f** Schematic band diagram of CZTSSe (**e**) without and (**f**) with Na elements under planar, concave, convex bending states.  $E_{vac}$ ,  $E_F$ ,  $E_C$ , and  $E_V$  are vacuum, Fermi, conduction, valence level, respectively.

bending state was  $-0.008$  and  $0.003$  eV, respectively, and that of Na-doped CZTSSe in concave and convex bending state was  $-0.008$  and  $0.008$  eV, respectively. The band gap of CZTS under biaxial strains can be changed significantly however, the change rate of band gap due to bending of polycrystalline thin film was smaller than 1% of their initial band gap for both samples<sup>31</sup>. Changes in band gap varied with the direction of the bending since the type of the strain (either tensile or compressive) is determined by the increase or decrease of the lattice constant.

Figure 1c, d shows the work function and valence band maximum (VBM) obtained from ultra-violet photoelectron spectroscopy (UPS). The work function of Na-doped CZTSSe was slightly smaller than that of undoped CZTSSe due to the surface dipoles induced by Na<sup>32</sup>. Both samples showed a decrement in work function under a concave bending state. However, the work function of Na-doped CZTSSe increased in the convex bending state, while that of Na-undoped CZTSSe decreased slightly. Energy from the Fermi level to the valence band edge (i.e., VBM) is larger in the Na-doped CZTSSe sample compared with Na-undoped CZTSSe because Na moves the Fermi level. The VBM relative to Fermi energy in planar state Na-doped CZTS is larger than Na-undoped CZTS because Fermi level in CZTS with substitutional Na<sub>Cu</sub> sites shift upward<sup>33,34</sup>. In both Na-doped and undoped CZTSSe, concave bending lowered the VBM, and that of Na-undoped CZTSSe lowered greater than Na-doped CZTSSe. In contrast, the VBM of Na-doped and undoped CZTSSe lowered slightly in the convex bending state.

Deformation of electronic band structure occurs different by direction of the bending (concave and convex). Figure 1e, f presents the schematic band structure of CZTSSe under planar, concave, and convex bending state. The valence band edge of Na-undoped CZTSSe was much lower than that of Na-doped CZTSSe in a concave bending state. Additionally, an upward shift of the Fermi level can limit the quasi-Fermi level splitting. In the convex bending state, the Fermi level of Na-doped CZTSSe located lower

than in Na-undoped CZTSSe resulted in larger quasi-Fermi level splitting. Deformation in the electronic structure of absorber materials can affect the band alignment at the interface and thus transport of charge carriers<sup>35,36</sup>. The Tauc plot, work function, and VBM variations of the CZTSSe samples with the NaF layer inserted in the various positions are presented in Supporting Information (Supplementary Figs. 2, 3).

### Electrical properties of CZTSSe under mechanical bending

We investigated the distribution of the contact potential difference ( $V_{CPD}$ ) of the CZTSSe absorber to understand the changes in the carrier transport properties of the CZTSSe absorber under mechanical stress. Figure 2a shows a simple diagram of the Kelvin probe force microscopy (KPFM) setup that was used to conduct measurements using concave and convex disks, which enabled mechanical bending stress to be applied to the CZTSSe thin-film solar cells during the KPFM measurements. The CZTSSe absorber on the flexible Mo substrate was bent by attaching the sample to a bending disk with a 20.47 mm bending radius. Figure 2b–l shows the surface topography and  $V_{CPD}$  map of the CZTSSe absorber surface in the planar, concave, and convex states. The surface topography of Na-doped CZTSSe demonstrated improvement in grain uniformity compared with that of undoped CZTSSe, as demonstrated in previous results<sup>37,38</sup>. Neither of the CZTSSe samples exhibited severe cracks or gaps induced by bending between or across the grains on their surfaces (see Fig. 2b–l and Supplementary Fig. 4).

The difference in the  $V_{CPD}$  value between the GBs and IG regions of CZTSSe surface with and without Na was positive (Fig. 2m, n). The local variation in the  $V_{CPD}$  is presented as a line profile in Supplementary Figure 5, showing that a higher  $V_{CPD}$  was produced near the GBs compared with that near the IG regions in both CZTSSe samples with and without Na. It implies that the  $V_{CPD}$  bent upward at the GBs, and the higher potential formed a local

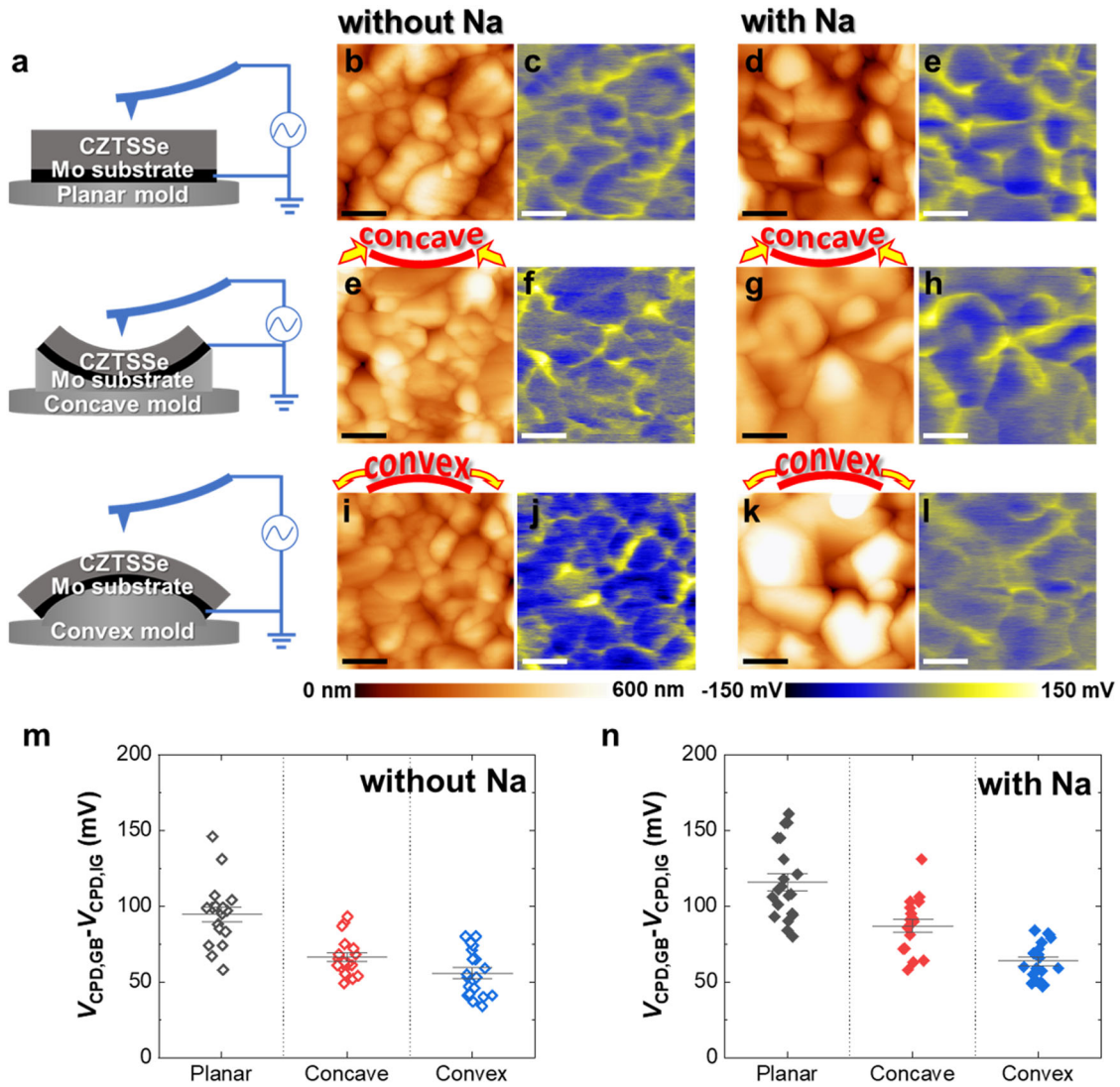


**Fig. 2** Distribution of contact potential difference in various bending modes. **a** Diagram representing the KPFM setup in the planar and bending modes. **b–l** Surface topography (**b, d, e, g, i, k**) and contact potential difference ( $V_{CPD}$ ) map (**c, e, f, h, j, l**) of Na-undoped and doped CZTSSe absorber material in the planar state and the concave and convex bending modes with a bending radius of 20.47 mm. (scale bar: 1  $\mu$ m) **m, n** Distribution of  $V_{CPD}$  difference between the intra-grain (IG) regions and grain boundaries (GBs) of Na-undoped (**m**) and doped (**n**) CZTSSe absorber material in the planar state and the concave and convex bending states. The CZTSSe absorber doped with Na displayed greater carrier separation at the GBs than the CZTSSe absorber without Na.

built-in potential in the vicinity of the GBs.  $V_{CPD}$  is defined as the work function difference between the tip and the sample, as follows:

$$V_{CPD} = \frac{\Phi_{tip} - \Phi_{sample}}{-e} \quad (1)$$

where  $\Phi_{tip}$  denotes the work function of the metal tip and  $\Phi_{sample}$  corresponds to the work function of the sample. Therefore, a higher  $V_{CPD}$  near the GBs indicates a larger work function near the GBs, resulting in upward band bending at the GBs. Upward potential bending near the GBs (i.e., upward band bending near the GBs) acts as an electron barrier. The electron barrier at the GBs repelled the minority carriers, which are the electrons in the  $p$ -type CZTSSe thin-film, from the GBs. The repulsion of electrons from the GBs prevents the recombination of carriers at defects in the GBs and lowers the recombination rate by lowering the Fermi levels closer to the valence band. Previous studies reported the occurrence of upward band bending near the GBs of metal-precursor CZTSSe thin film<sup>39,40</sup>. Particularly, Ma et al. demonstrated that the upward bending of the conduction band edge in

the CZTSSe thin film is beneficial in reducing recombination at the GBs by repelling electrons from the GBs<sup>41</sup>. Consequently, enhanced band bending increases the barrier height at GBs improving the charge separation by reducing the recombination of the charge carriers.

The difference in the  $V_{CPD}$  value in the planar state between the GBs and IG regions of Na-doped CZTSSe was larger than that of CZTSSe without Na, showing the enhanced band bending. Our previous study revealed that doping the CZTSSe absorber layer with Na promoted carrier separation at the GBs, which can improve cell performance<sup>28,42,43</sup>. We reported that the defects generated in the metal-precursor CZTSSe grown at low temperature primarily had acceptor defects, such as  $V_{Cu}^{-1}$ ,  $V_{Zn}^{-1}$ ,  $Cu_{Zn}^{-1}$ , and  $Zn_{Sn}^{-1}$ . They introduced negatively charged sites at the GBs, resulting in upward band bending<sup>28,30</sup>. Additionally, the incorporated Na accumulated along the GBs because the diffusion of Na towards the IG regions was limited by the sulfo-selenization process of CZTSSe<sup>37</sup>. The incorporation of Na enables  $Na_{Zn}$  shallow acceptor defects to be formed owing to their low formation



energy<sup>44</sup>. This Na-related shallow acceptor has a negative charge, which also gives rise to the creation of negatively charged sites at the GBs.

Stress-induced space-charge transport was observed with band bending at the GBs. Figure 2m, n shows 18  $V_{CPD}$  values that were extracted from the GBs and IG regions in the planar, concave, and convex states. The mechanical stress altered the distribution of the  $V_{CPD}$  values. The value of the  $V_{CPD}$  between the GBs and IG regions was found to be positive in the concave and convex bending modes for both the Na-doped and undoped CZTSSe absorbers. However, the average difference in the  $V_{CPD}$  value between the GBs and IG regions decreased in the concave and convex bending modes. The  $V_{CPD}$  difference between GBs and IGs was significantly reduced in both the Na-doped and undoped CZTSSe samples in the convex state compared to the concave state. Less degradation in  $V_{CPD}$  difference under the concave bending state shows that carrier transport on the surface was maintained compared to the convex bending state. Additionally, the reduction in  $V_{CPD}$  bending under the mechanical bending state occurred significantly in Na-undoped CZTSSe than in Na-doped CZTSSe.

The decrease in the charge barrier height weakened the carrier separation, which increased the recombination of the carriers at the GBs<sup>45</sup>. Therefore, the electrons or holes were not effectively repelled or collected at the GBs under the bending states due to the decreased band bending resulting in weak carrier separation. The band bending structure at the GBs is highly affected by the defect charges located at the GBs. Decreased band bending implies that the defect charges were changed due to mechanical bending. However, the type of strain-induced defects cannot be identified by KPFM, suggesting the need for further studies on the strain-induced defects in kesterite. In addition, flexoelectric effect could be generated with the strain as probing the bent kesterite materials which adopt a centrosymmetric space group<sup>46,47</sup>. However, the flexoelectric effect was not handled here as it is hardly observed due to its extremely small magnitude in the bulk samples<sup>47</sup>.

### Loss mechanism of open-circuit voltage under mechanical stress

The CZTSSe absorber was examined using photo-assisted KPFM to investigate the changes in the photogenerated electrical properties of the CZTSSe under the mechanical stress. Figure 3a–h shows the surface topography and local  $V_{OC}$  variation map of CZTSSe with (a–d) and without (e–h) Na in the convex and concave bending modes. A red laser with a wavelength of 650 nm (i.e., 1.91 eV) with 100 mW power was used to excite the carriers on the sample surface. The local  $V_{OC}$  variation map in Fig. 3a–h shows a large surface photo-voltage (SPV) distribution at the GBs, which are indicated by the bright regions. The illumination-induced change in the  $V_{CPD}$  is the SPV, defined as the difference between the  $V_{CPD}$  under illuminated and dark conditions (see Supplementary Fig. 6).

Figure 3i shows the changes in the  $V_{CPD}$  under illumination (i.e., SPV) with mechanical stress. Additionally, the SPV is related to the local  $V_{OC}$  loss mechanism, which explains the decrease in the device parameters owing to mechanical stress. The relationship between the  $V_{CPD}$  and local  $V_{OC}$  is as follows<sup>48</sup>:

$$\Delta V_{OC,local} = \frac{\Delta E_{quasi-Fermi}}{q} = V_{CPD,illuminated} - V_{CPD,dark} = SPV \quad (2)$$

Tennyson et al. demonstrated a correlation between the partially resolved  $V_{OC}$  obtained from the SPV and device  $V_{OC}$ <sup>48</sup>. The local  $V_{OC}$  can be resolved by the local quasi-Fermi level splitting, which can be determined by measuring the  $V_{CPD}$  difference between the illuminated and dark states, denoted as the SPV, as shown in Eq. (2). Additionally, a previous study

revealed that the  $V_{OC}$  of the device is proportional to the SPV upon illumination of the organic photovoltaic device<sup>49</sup>.

Fundamentally, SPV formation is limited by photogenerated electron–hole recombination<sup>50,51</sup>. The defects suppressed the SPV generation in the CZTSSe absorber without Na, indicating the poor transport of photogenerated carriers. Defects in the CZTSSe thin film can lower the  $V_{OC}$  by acting as recombination centers forming a mid-gap state or non-uniform chemical stoichiometry and reducing band bending near p–n junction<sup>52–55</sup>. Our previous study demonstrated that the SPV generation is maximized in the CZTSSe thin film for an optimal Na content owing to the passivation of defect sites<sup>56</sup>. Additionally, the effective mass of holes can be reduced by Na doping, and the lighter photogenerated carriers favor the separation of electron–hole pairs<sup>33</sup>.

Interestingly, the generated SPV decreased with the mechanical stress. The SPV of the CZTSSe samples with and without Na decreased with mechanical bending, implying alteration of the recombination process and device properties under mechanical stress. SPV results in bending mode indicate the occurrence of greater recombination of photogenerated charge carriers, related to the  $V_{OC}$  loss, in the convex than in the concave bending mode. An increase in the recombination of photogenerated charge carriers can be attributed to strain-induced defects, which can explain the electronic band structure change. Kahlaoui et al. reported that the tensile strain on CZTS crystals makes the bonds fragile, facilitating their breaking by increasing the interatomic distance<sup>57</sup>. Additionally, the decrease in the SPV was small in CZTSSe with Na doping; it indicates that improved carrier transport by Na was maintained even under the mechanical bending state, consistent with  $V_{CPD}$  change results. The dispersion of the SPV distribution in Na-doped CZTSSe with mechanical bending was larger than that of Na-undoped CZTSSe because some GBs in Na-doped CZTSSe still maintained large SPV under stress.

Figure 3j, k shows the carrier transport mechanism and the corresponding band diagrams for the planar, concave, and convex bending modes under illumination. In Fig. 3j, the black and red lines indicate the band bending between the dark and illuminated states (650 nm wavelength laser, as mentioned above), respectively. Charge carriers in the CZTSSe under the planar states separated due to the large charge barrier at the GBs. In contrast, the photogenerated charge carriers in the CZTSSe under the bending states recombined as the charge barrier decreases, resulting in less SPV than in the planar states. In Fig. 3k, the band bending in the energy band diagram emerges when the metal tip and the surface of the CZTSSe absorber come in contact. The generated SPV exceeded 100 mV in the planar state, resulting in band flattening and large quasi-Fermi level splitting, as shown in Fig. 3k. However, the SPV was limited in the bending mode owing to the recombination of the photogenerated carriers, especially under the convex bending mode. Recombination of the photogenerated carriers due to the strain-induced defects could be attributed to less band bending at the surface under the stress.

### Performance and stability of flexible CZTSSe devices

Table 1 lists the photovoltaic device parameters of samples. The device with the NaF layer demonstrated a higher PCE of 11.19% compared to that of the CZTSSe sample without Na. The other photovoltaic device parameters of the Na-doped device, such as the fill factor (FF),  $V_{OC}$ , and short-circuit current density ( $J_{SC}$ ), improved compared with the undoped device. Especially, FF and  $V_{OC}$  improved significantly, while improvement in  $J_{SC}$  with Na doping was marginal (0.82 mA cm<sup>-2</sup>). The photovoltaic device parameters of the flexible CZTSSe samples with the NaF layer inserted at various positions are shown in Supplementary Table 1 of the Supporting Information.

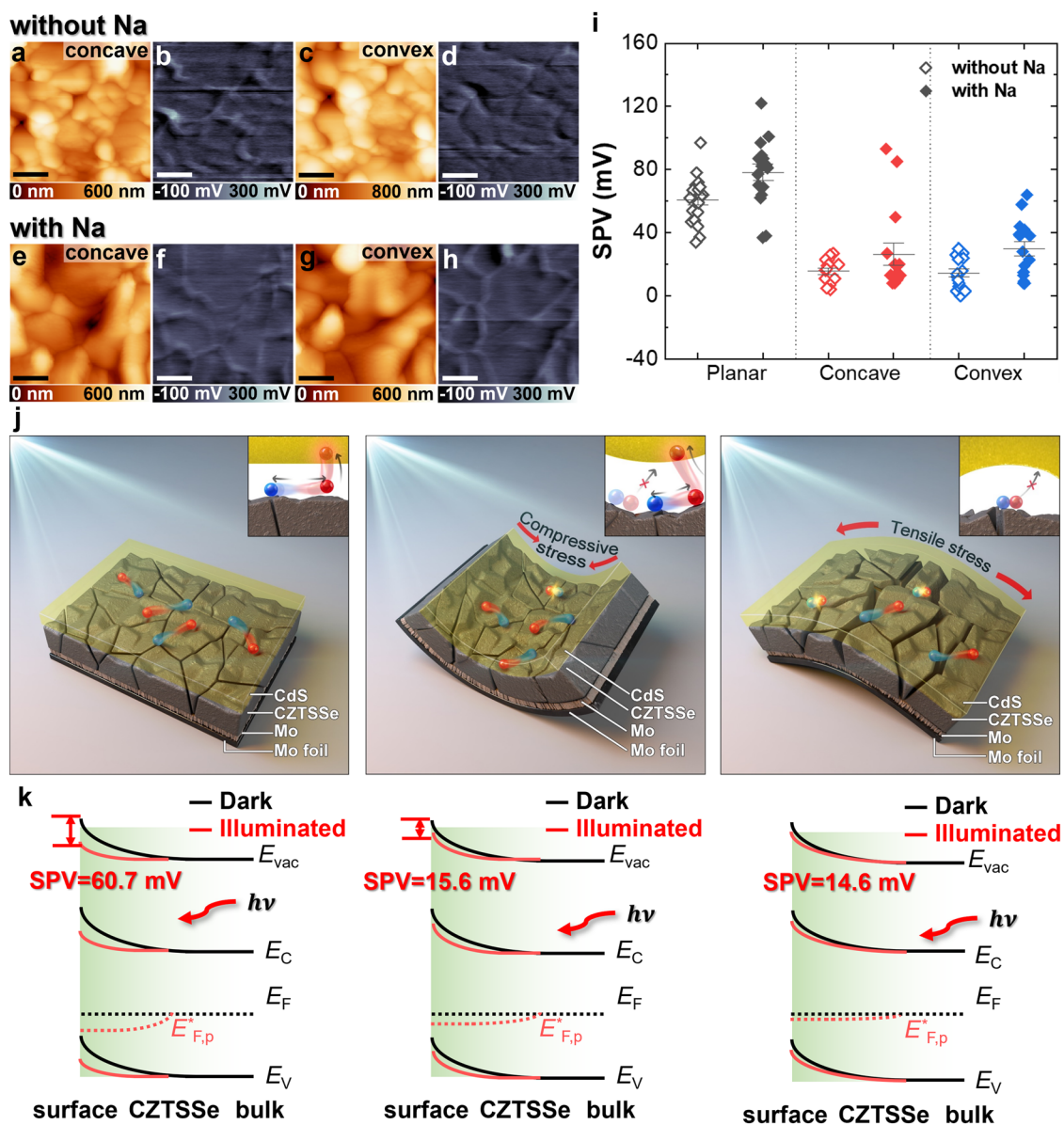


**Fig. 3**  $V_{oc}$  loss of the CZTSSe thin film in different bending modes. **a–h** Surface topography (**a, c, e, g**) and local  $V_{oc}$  variation map (**b, d, f, h**) of Na-undoped and doped CZTSSe in the concave and convex states. (scale bar: 1  $\mu$ m) **i** Surface photo-voltage (SPV) at GBs for CZTSSe with and without Na. **j** Diagrams of the polycrystalline CZTSSe grains under planar, concave, and convex bending states. The red and blue spheres indicate electrons and holes, respectively. **k** Schematic band diagrams of the CZTSSe under the dark state and illuminated condition with the generation of SPV.

**Table 1.** Photovoltaic device parameters of CZTSSe thin-film solar cells with and without Na.

Sample	Precursor structure	$V_{oc}$ [V]	$J_{sc}$ [ $\text{mA cm}^{-2}$ ]	FF [%]	PCE [%]
CZTSSe without Na	Sn/Cu/Zn/Mo/Mo foil	0.497	32.25	44.54	7.14
CZTSSe with Na	Sn/NaF/Cu/Zn/Mo/Mo foil	0.539	33.07	62.79	11.19

Figure 4a, b shows the rates at which the photovoltaic device parameters changed after concave and convex bending. The devices were subjected to a bending test with a bending radius of 50 mm and a maximum of 1000 bending cycles. The photovoltaic device parameters were measured at four points on the two devices after the bending test. The average rate of change was compared with that of the unbent device which is set zero. The performance of the photovoltaic device declined after the bending test, which suggests that the convex bending mode

has an adverse effect, whereas the effect of the concave bending mode is less severe than in the convex bending. Deng et al. demonstrated that the degradation of PCE at the surface subjected to the convex bending in a bifacial flexible CZTSSe device was more significant than that at the surface subjected to the concave bending as the crystalline structure was damaged<sup>58</sup>. After 1000 bending cycles, the decrease in the PCE was  $-6.82\%$  and  $-9.13\%$  for concave and convex bending, respectively, showing that more than 90% of the PCE was maintained after

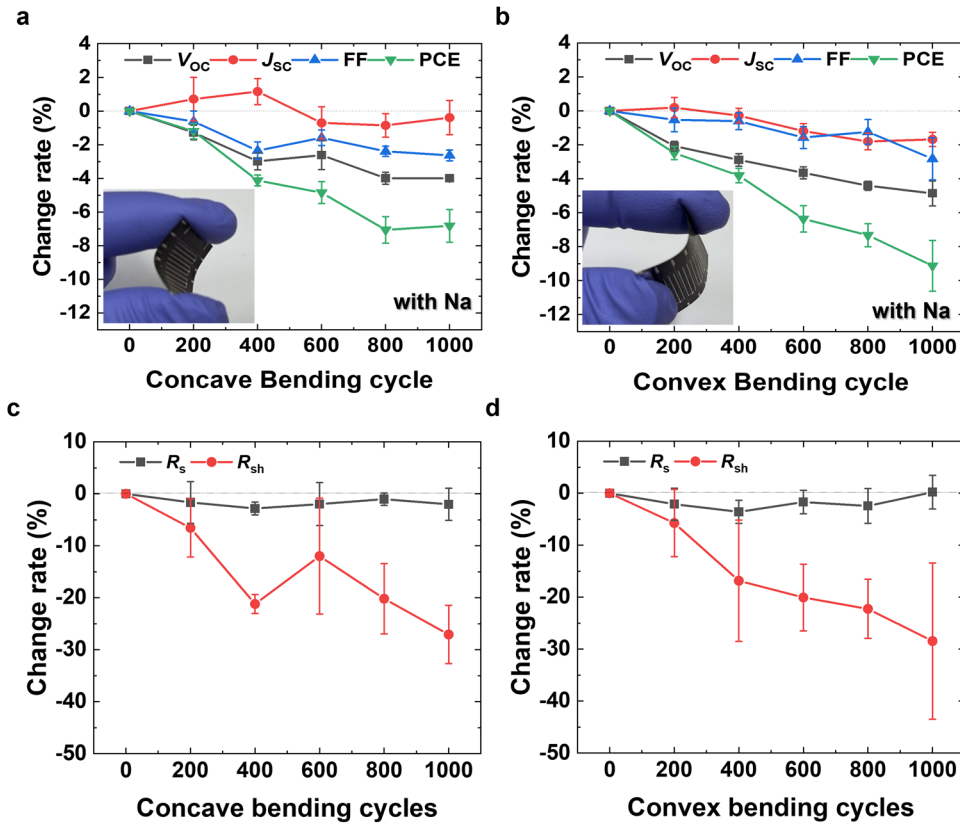


**Fig. 4** Changes in photovoltaic device parameter by mechanical bending test. **a, b** Rate of change of photovoltaic device parameters with concave (**a**) and convex (**b**) bending with a bending radius of 50 mm and a maximum of 1000 bending cycles. Photovoltaic device parameters were measured after 200, 400, 600, 800, and 1000 bending cycles. The inset in (**a, b**) shows an image of the bent device. **c, d** Rate of change of series and shunt resistance with concave (**c**) and convex (**d**) bending with the same bending condition. Error bars in (**a–d**) are defined as standard deviation of photovoltaic parameters obtained from four points of two devices.

the bending test. Jeong et al. also demonstrated that flexible CZTSSe thin-film solar cells using Mo metal foil maintained over 90% of their initial PCE after the bending test with a bending radius of more than 3 mm<sup>29</sup>. The rates at which the  $V_{oc}$ ,  $J_{sc}$ , and FF changed after 1000 convex bending cycles were  $-4.86$ ,  $-1.68$ , and  $-2.83\%$ , respectively, whereas, after 1000 concave bending cycles, the rates were  $-3.99$ ,  $-0.39$ , and  $-2.64\%$ , respectively. The negative rate of change of the  $V_{oc}$  was more substantial than that of the  $J_{sc}$ . Hence, the decrease in  $V_{oc}$  may be the main reason for the degradation in the performance of the photovoltaic device. The  $V_{oc}$  is influenced by the band gap therefore, the decrease in severe  $V_{oc}$  after bending can be affected by the strain-induced band gap change of the absorber materials, as demonstrated in Fig. 1a, b.

The rate of change of series and shunt resistance under concave and convex bending states are shown in Fig. 4c, d, respectively. The change rates of series resistance after 1000 bending cycles were  $-2.03$  and  $0.20\%$  in the concave and convex bendings, respectively, which were not significantly affected by the bending direction. On the contrary, the change rates of shunt resistance showed a significant decrease of  $-27.07$  and  $-28.45\%$  after the concave and convex bendings, respectively. In fact, only a few papers have reported the bending properties of kesterite solar cells. One study demonstrated that the voids at the CZTS/Mo interface might be damaged by convex bending, resulting in the formation of a shunt path, an increase in series resistance, and a decrease in shunt resistance<sup>59</sup>.

This study focused on the degradation of the device performance under mechanical bending and considered the

photoexcited characteristics and the influence of energy band structure. The correlation between the surface charge transport and morphological changes in the GBs should be studied in the future.

We studied the deformation of electronic band structure and electrical properties of a highly efficient flexible kesterite CZTSSe photovoltaic device with and without artificial Na doping under mechanical stress. The band gap of CZTSSe decreased and increased in the concave and convex bending state, respectively. Fermi level shift up or downward in mechanical bending states, which can affect the band alignment. The electrical properties of the CZTSSe absorber layer, to which mechanical stress was applied, were investigated by KPFM. The results showed that the height of the electron barrier decreased under mechanical stress; the carrier separation at GBs weakened, which can result in carrier recombination. The loss of local  $V_{oc}$  increased under mechanical stress, was measured by SPV, revealing a significant charge carrier recombination occurred under a convex bending state than under a concave bending state. The local  $V_{oc}$  loss under mechanical stress was consistent with the substantial decrement in the device  $V_{oc}$  observed in the concave and convex bending tests. In conclusion, the degradation of carrier transport was greater in the convex bending state than in the concave bending state. Furthermore, CZTSSe with Na doping showed less degradation than Na-free CZTSSe. Specially, we developed a powerful characterization method verifying the surface charge transport of the bent materials, which can be applied to any other flexible devices, such as silicon, CIGS, and perovskite solar cells, beyond the flexible kesterite solar cells.



## METHODS

### Fabrication

The CZTSSe thin-film solar cell consisted of the following: a 0.1-mm-thick Mo-foil substrate (MTI Co.), CZTSSe absorber fabricated via sputtering, 50-nm-thick CdS buffer layer deposited via chemical bath deposition, 50-nm-thick intrinsic ZnO layer deposited by radio-frequency (RF) sputtering, 300-nm-thick Al-doped ZnO (AZO) layer as a transparent conducting oxide deposited via sputtering, and 500-nm-thick Al collection grid deposited via thermal evaporation. Among the five different precursor structures, four contained an additional NaF layer that was inserted at different positions in the metallic-precursor stack, whereas one precursor structure did not contain the NaF layer. The structures were as follows: Sn/Cu/Zn/Mo/Mo-foil (CZTSSe1), Sn/Cu/Zn/NaF/Mo/Mo foil (CZTSSe2), Sn/Cu/NaF/Zn/Mo/Mo foil (CZTSSe3), Sn/NaF/Cu/Zn/Mo/Mo foil (CZTSSe4), and NaF/Sn/Cu/Zn/Mo/Mo foil (CZTSSe5). The Mo back contact layer was coated onto the Mo-foil substrate<sup>16</sup>. Furthermore, Cu, Zn, and Sn sputtering targets of 99.99% purity were used for metal-precursor sputtering. The sputtering power was 150 W, 300 W, and 300 W direct current (DC) for 630, 115, and 260 s, respectively, in an Ar atmosphere pressurized to 1 mTorr. Thermal evaporation was used to deposit the 10-nm-thick NaF layer while fabricating the four precursor structures with the NaF layer. The precursors were sulfo-selenized with diluted H<sub>2</sub>S gas with 90 vol% Ar as the S source and Se pellets (Sigma-Aldrich) as the Se source in a rapid thermal process (RTP) chamber. The RTP chamber was filled with 250 sccm H<sub>2</sub>S and 2000 sccm Ar gas under 700 Torr pressure. Se pellets (0.37 g) were introduced to the RTP chamber with a volume of 18375 cm<sup>3</sup>. After that, the precursors were heated from room temperature to 300 °C for 560 s; this temperature level was maintained for 900 s. Subsequent heating for 1800 s raised the temperature to 480 °C, and the temperature was maintained at this level for 600 s. The partial pressure of Se was changed during the sulfo-selenization process by the temperature profile; after that, the other layers were added.

### Characterization

The optical band gap was determined using the Kubelka-Munk function from diffuse reflectance spectra obtained by UV-Visible-NIR spectrophotometer (Cary5000, Agilent). For the UV-Visible-NIR spectroscopy, a beam size was minimized to 1 mm<sup>2</sup> and the area exposed to the beam was loaded at the same location to avoid any optical path difference due to the surface curvature. He I (21.2 eV) was used as an ultra-violet source for ultra-violet photoelectron spectroscopy (UPS) (Axis-Supra, Kratos). During the UV-Visible and UPS measurements, a homogeneous strain was maintained by attaching the samples to the bending molds. The spectrum was obtained from the area of 50 μm<sup>2</sup> therefore, we assumed that the height difference due to the curvature was neglectable for probing the area with the homogeneous strain. The surface structural and electrical properties of the films were analyzed using photo-assisted KPFM in ambient conditions. A commercial atomic force microscope (n-Tracer from NanoFocus Inc.) with a Pt/Ir-coated silicon cantilever (Nanosensors) was used for the amplitude modulation (AM)-mode KPFM measurements with an applied AC bias of 1.0 V. The topography and contact potential difference maps in the non-contact mode were obtained lifting the tip higher than 40 nm from the sample during the KPFM measurements to avoid the crossstalk effect. A flattening function was applied to the V<sub>CPD</sub> map to calibrate it from the reference point to zero. A red laser (wavelength of 650 nm, 1.91 eV) with a 100 mW power was used to excite the carriers on the CZTSSe surface and measure the SPV. The bending radius of the concave and convex molds was 20.47 mm. Furthermore, the current-voltage characteristics were determined under a simulated air mass with a 1.5 global (AM 1.5 G) spectrum and 100 mW cm<sup>-2</sup>

(1 sun) illumination at 25 °C using a 94022 A solar simulator (Newport Co.). The values of the photovoltaic device parameters after the bending test with 200, 400, 600, 800, and 1000 bending cycles and bending radii were maintained at 50 mm during the bending test. Concave and convex bending was applied to the cells at a speed of 1.0 mm s<sup>-1</sup> using the instruments.

### DATA AVAILABILITY

The authors declare that the data supporting the findings of this study are available within the paper and its supplementary information files.

Received: 23 July 2022; Accepted: 13 October 2022;

Published online: 01 November 2022

### REFERENCES

- Ahmed, A. et al. Additively manufactured nano-mechanical energy harvesting systems: advancements, potential applications, challenges and future perspectives. *Nano Converg.* **8**, 37 (2021).
- Hwang, I., Um, H.-D., Kim, B.-S., Woher, M. & Seo, K. Flexible crystalline silicon radial junction photovoltaics with vertically aligned tapered microwires. *Energy Environ. Sci.* **11**, 641–647 (2018).
- Chirila, A. et al. Potassium-induced surface modification of Cu(In,Ga)Se<sub>2</sub> thin films for high-efficiency solar cells. *Nat. Mater.* **12**, 1107–1111 (2013).
- Carron, R. et al. Advanced alkali treatments for high efficiency Cu(In,Ga)Se<sub>2</sub> solar cells on flexible substrates. *Adv. Energy Mater.* **9**, 1900408 (2019).
- Ramanujam, J. & Singh, U. P. Copper indium gallium selenide based solar cells—a review. *Energy Environ. Sci.* **10**, 1306–1319 (2017).
- Ru, P. et al. High electron affinity enables fast hole extraction for efficient flexible inverted perovskite solar cells. *Adv. Energy Mater.* **10**, 1903487 (2020).
- Feng, J. et al. Record efficiency stable flexible perovskite solar cell using effective additive assistant strategy. *Adv. Mater.* **30**, e1801418 (2018).
- Di Giacomo, F., Fakharuddin, A., Jose, R. & Brown, T. M. Progress, challenges and perspectives in flexible perovskite solar cells. *Energy Environ. Sci.* **9**, 3007–3035 (2016).
- Kim, S., Quy, H. V. & Bark, C. W. Photovoltaic technologies for flexible solar cells: beyond silicon. *Mater. Today Energy* **19**, 100583 (2021).
- Ramanujam, J. et al. Flexible CIGS, CdTe and a-Si:H based thin film solar cells: a review. *Prog. Mater. Sci.* **110**, 100619 (2020).
- Park, N.-G., Grätzel, M., Miyasaka, T., Zhu, K. & Emery, K. Towards stable and commercially available perovskite solar cells. *Nat. Energy* **1**, 16152 (2016).
- Ramasamy, K., Malik, M. A. & O'Brien, P. Routes to copper zinc tin sulfide Cu<sub>2</sub>ZnSnS<sub>4</sub> a potential material for solar cells. *Chem. Commun.* **48**, 5703–5714 (2012).
- Winkler, M. T. et al. Optical designs that improve the efficiency of Cu<sub>2</sub>ZnSn(S,Se)<sub>4</sub> solar cells. *Energy Environ. Sci.* **7**, 1029–1036 (2014).
- Wang, W. et al. Device characteristics of CZTSSe thin-film solar cells with 12.6% efficiency. *Adv. Energy Mater.* **4**, 1301465 (2014).
- Son, D.-H. et al. Effect of solid-H<sub>2</sub>S gas reactions on CZTSSe thin film growth and photovoltaic properties of a 12.62% efficiency device. *J. Mater. Chem. A* **7**, 25279–25289 (2019).
- Li, J. et al. Defect control for 12.5% efficiency Cu<sub>2</sub>ZnSnSe<sub>4</sub> kesterite thin-film solar cells by engineering of local chemical environment. *Adv. Mater.* **32**, e2005268 (2020).
- Kumar, M., Dubey, A., Adhikari, N., Venkatesan, S. & Qiao, Q. Strategic review of secondary phases, defects and defect-complexes in kesterite CZTS–Se solar cells. *Energy Environ. Sci.* **8**, 3134–3159 (2015).
- Schorr, S. et al. Point defects, compositional fluctuations, and secondary phases in non-stoichiometric kesterites. *J. Phys.: Energy* **2**, 012002 (2019).
- Brammertz, G. et al. Characterization of defects in 9.7% efficient Cu<sub>2</sub>ZnSnSe<sub>4</sub>-CdS-ZnO solar cells. *Appl. Phys. Lett.* **103**, 163904 (2013).
- Grossberg, M., Raadik, T., Raudoja, J. & Krustok, J. Photoluminescence study of defect clusters in Cu<sub>2</sub>ZnSnS<sub>4</sub> polycrystals. *Curr. Appl. Phys.* **14**, 447–450 (2014).
- Xie, W. et al. 10.24% Efficiency of flexible Cu<sub>2</sub>ZnSn(S,Se)<sub>4</sub> solar cells by pre-evaporation selenization technique. *Small* **18**, e2201347 (2022).
- Haass, S. G. et al. Complex interplay between absorber composition and alkali doping in high-efficiency kesterite solar cells. *Adv. Energy Mater.* **8**, 015133 (2018).
- Gershon, T. et al. The role of sodium as a surfactant and suppressor of non-radiative recombination at internal surfaces in Cu<sub>2</sub>ZnSnS<sub>4</sub>. *Adv. Energy Mater.* **5**, 1400849 (2015).

24. Hsieh, Y. T. et al. Efficiency enhancement of  $\text{Cu}_2\text{ZnSn}(\text{S,Se})_4$  solar cells via alkali metals doping. *Adv. Energy Mater.* **6**, 1502386 (2016).
25. Yang, K. J. et al. Flexible  $\text{Cu}_2\text{ZnSn}(\text{S,Se})_4$  solar cells with over 10% efficiency and methods of enlarging the cell area. *Nat. Commun.* **10**, 2959 (2019).
26. López-Marino, S. et al. Alkali doping strategies for flexible and light-weight  $\text{Cu}_2\text{ZnSnSe}_4$  solar cells. *J. Mater. Chem. A* **4**, 1895–1907 (2016).
27. Yan, Q. et al. High flexible  $\text{Cu}_2\text{ZnSn}(\text{S,Se})_4$  solar cells by green solution-process. *Sol. Energy* **177**, 508–516 (2019).
28. Yang, K.-J. et al. The alterations of carrier separation in kesterite solar cells. *Nano Energy* **52**, 38–53 (2018).
29. Jeong, W. L. et al. Impact of Na doping on the carrier transport path in polycrystalline flexible  $\text{Cu}_2\text{ZnSn}(\text{S,Se})_4$  solar cells. *Adv. Sci.* **7**, 1903085 (2020).
30. Yang, K. J. et al. Sodium effects on the diffusion, phase, and defect characteristics of kesterite solar cells and flexible  $\text{Cu}_2\text{ZnSn}(\text{S,Se})_4$  with greater than 11% efficiency. *Adv. Funct. Mater.* **31**, 2202238 (2021).
31. Li, C.-R. et al. Electronic and optical properties of kesterite  $\text{Cu}_2\text{ZnSnS}_4$  under in-plane biaxial strains: first-principles calculations. *Phys. Lett. A* **377**, 2398–2402 (2013).
32. Heske, C., Fink, R., Umbach, E., Riedl, W. & Karg, F. Na-induced effects on the electronic structure and composition of  $\text{Cu}(\text{In,Ga})\text{Se}_2$  thin-film surfaces. *Appl. Phys. Lett.* **68**, 3431–3433 (1996).
33. Zhao, Z. Y. & Zhao, X. First-principles study on doping effects of sodium in kesterite  $\text{Cu}_2\text{ZnSnS}_4$ . *Inorg. Chem.* **53**, 9235–9241 (2014).
34. Liu, B. et al. Effect of Na doping on the performance and the band alignment of CZTS/CdS thin film solar cell. *Sol. Energy* **201**, 219–226 (2020).
35. Guo, H. et al. Band-gap-graded  $\text{Cu}_2\text{ZnSn}(\text{S,Se})_4$  drives highly efficient solar cells. *Energy Environ. Sci.* **15**, 693–704 (2022).
36. Lee, J., Khan, M. E. & Kim, Y. H. Quantum hybridization negative differential resistance from non-toxic halide perovskite nanowire heterojunctions and its strain control. *Nano Converg.* **9**, 25 (2022).
37. Sutter-Fella, C. M. et al. Sodium assisted sintering of chalcogenides and its application to solution processed  $\text{Cu}_2\text{ZnSn}(\text{S,Se})_4$  thin film solar cells. *Chem. Mater.* **26**, 1420–1425 (2014).
38. Sun, K. et al. Flexible kesterite  $\text{Cu}_2\text{ZnSnS}_4$  solar cells with sodium-doped molybdenum back contacts on stainless steel substrates. *Sol. Energy Mater. Sol. Cells* **182**, 14–20 (2018).
39. Kim, J. et al. High photo-conversion efficiency  $\text{Cu}_2\text{ZnSn}(\text{S,Se})_4$  thin-film solar cells prepared by compound-precursors and metal-precursors. *Sol. Energy Mater. Sol. Cells* **183**, 129–136 (2018).
40. Vishwakarma, M., Agrawal, K., Hadermann, J. & Mehta, B. R. Investigating the effect of sulphurization on volatility of compositions in Cu-poor and Sn-rich CZTS thin films. *Appl. Surf. Sci.* **507**, 145043 (2020).
41. Ma, Y. et al. Band bending near grain boundaries of  $\text{Cu}_2\text{ZnSn}(\text{S,Se})_4$  thin films and its effect on photovoltaic performance. *Nano Energy* **51**, 37–44 (2018).
42. Kim, J. et al. Sodium-assisted passivation of grain boundaries and defects in  $\text{Cu}_2\text{ZnSnSe}_4$  thin films. *Phys. Chem. Chem. Phys.* **22**, 7597–7605 (2020).
43. Kim, G. Y. et al. Nanoscale investigation of surface potential distribution of  $\text{Cu}_2\text{ZnSn}(\text{S,Se})_4$  thin films grown with additional NaF layers. *Nano Converg.* **1**, 27 (2014).
44. Han, M., Zhang, X. & Zeng, Z. An investigation of Na-related defects in  $\text{Cu}_2\text{ZnSnSe}_4$ . *Phys. Chem. Chem. Phys.* **19**, 17799–17804 (2017).
45. Park, J. et al. Investigation of low intensity light performances of kesterite CZTSe, CZTSSe, and CZTS thin film solar cells for indoor applications. *J. Mater. Chem. A* **8**, 14538–14544 (2020).
46. Yang, M.-M., Kim, D. J. & Alexe, M. Flexo-photovoltaic effect. *Science* **360**, 904–907 (2018).
47. Zou, H., Zhang, C., Xue, H., Wu, Z. & Wang, Z. L. Boosting the solar cell efficiency by flexo-photovoltaic effect? *ACS Nano* **13**, 12259–12267 (2019).
48. Tennyson, E. M. et al. Nanoimaging of open-circuit voltage in photovoltaic devices. *Adv. Energy Mater.* **5**, 1501142 (2015).
49. Shao, G., Glaz, M. S., Ma, F., Ju, H. & Ginger, D. S. Intensity-modulated scanning kelvin probe microscopy for probing recombination in organic photovoltaics. *ACS Nano* **8**, 10799 (2014).
50. Zhang, Z. & Yates, J. T. Jr. Band bending in semiconductors: chemical and physical consequences at surfaces and interfaces. *Chem. Rev.* **112**, 5520–5551 (2012).
51. Chen, R., Fan, F., Dittrich, T. & Li, C. Imaging photogenerated charge carriers on surfaces and interfaces of photocatalysts with surface photovoltage microscopy. *Chem. Soc. Rev.* **47**, 8238–8262 (2018).
52. Chen, S., Walsh, A., Gong, X. G. & Wei, S. H. Classification of lattice defects in the kesterite  $\text{Cu}_2\text{ZnSnS}_4$  and  $\text{Cu}_2\text{ZnSnSe}_4$  earth-abundant solar cell absorbers. *Adv. Mater.* **25**, 1522–1539 (2013).
53. Duan, H.-S. et al. The role of sulfur in solution-processed  $\text{Cu}_2\text{ZnSn}(\text{S,Se})_4$  and its effect on defect properties. *Adv. Funct. Mater.* **23**, 1466–1471 (2013).
54. Cui, C. et al. Surface defect ordered  $\text{Cu}_2\text{ZnSn}(\text{S,Se})_4$  solar cells with efficiency over 12% via manipulating local substitution. *J. Energy Chem.* **67**, 555–562 (2022).
55. Karade, V. C. et al. Understanding defects and band tailing characteristics and their impact on the device performance of  $\text{Cu}_2\text{ZnSn}(\text{S,Se})_4$  solar cells. *J. Mater. Chem. A* **10**, 8466–8478 (2022).
56. Park, H. K. et al. Chemical tailoring of sodium content for optimization of interfacial band bending and alignment in flexible kesterite solar cells. *Sol. Energy Mater. Sol. Cells* **230**, 111243 (2021).
57. Kahlaoui, S., Belhorma, B., Labrim, H., Boujnah, M. & Regragui, M. Strain effects on the electronic, optical and electrical properties of  $\text{Cu}_2\text{ZnSnS}_4$ : DFT study. *Heliyon* **6**, e03713 (2020).
58. Deng, H. et al. Novel symmetrical bifacial flexible CZTSSe thin film solar cells for indoor photovoltaic applications. *Nat. Commun.* **12**, 3107 (2021).
59. Peng, C.-Y. et al. Fabrication of  $\text{Cu}_2\text{ZnSnS}_4$  solar cell on a flexible glass substrate. *Thin Solid Films* **562**, 574–577 (2014).

## ACKNOWLEDGEMENTS

This research was supported by the Basic Science Research Program through the National Research Foundation of Korea (NRF) funded by the Ministry of Education (NRF-2018R1A6A1A03025340) and Ministry of Science, Technology, ICT, and Future Planning (NRF-2021R1A2B5B02001961). This research was supported by the program of Phased development of carbon neutral technologies through the National Research Foundation of Korea (NRF) funded by the Ministry of Science, ICT (NRF-2022M3J1A1064229). Additionally, this work was supported by the DGIST R&D programs of the Ministry of Science and ICT (22-CoE-ET-01). The first author, H.K. Park, is also grateful for the financial support received from the Hyundai Motor Chung Mong-Koo Foundation.

## AUTHOR CONTRIBUTIONS

H.K.P. designed the research and performed the UPS, UV-Visible, KPFM, and SPV measurements. Y.C. contributed to the KPFM and SPV measurements and discussion. J.K. contributed to the KPFM and SPV measurements and discussions. J.K. supervised the bending *IV* measurement, and S.K. performed the bending *IV* measurements. K.-J.Y., D.-H.K., and J.-K.K. designed the fabrication of the flexible CZTSSe solar cells. K.-J.Y. and S.K. contributed to *IV* measurements. The manuscript was mainly written by the first author, H.K.P. W.J. designed the research and supervised the overall work. All authors discussed the results and commented on the manuscript.

## COMPETING INTERESTS

The authors declare no competing interests.

## ADDITIONAL INFORMATION

**Supplementary information** The online version contains supplementary material available at <https://doi.org/10.1038/s41528-022-00221-4>.

**Correspondence** and requests for materials should be addressed to Kee-Jeong Yang or William Jo.

**Reprints and permission information** is available at <http://www.nature.com/reprints>

**Publisher's note** Springer Nature remains neutral with regard to jurisdictional claims in published maps and institutional affiliations.



**Open Access** This article is licensed under a Creative Commons Attribution 4.0 International License, which permits use, sharing, adaptation, distribution and reproduction in any medium or format, as long as you give appropriate credit to the original author(s) and the source, provide a link to the Creative Commons license, and indicate if changes were made. The images or other third party material in this article are included in the article's Creative Commons license, unless indicated otherwise in a credit line to the material. If material is not included in the article's Creative Commons license and your intended use is not permitted by statutory regulation or exceeds the permitted use, you will need to obtain permission directly from the copyright holder. To view a copy of this license, visit <http://creativecommons.org/licenses/by/4.0/>.

© The Author(s) 2022